Nigerian Journal of Physics (NJP)
ISSN online: 3027-0936
ISSN print: 1595-0611
DOI: https://doi.org/10.62292/njp.v35i3.2026.637
Volume 35(3), September 2026

Performance Optimisation and Stability Assessment of ITO/ZnO/PM6:ITIC/PEDOT: PSS/Graphene Organic Solar Cell: A Comprehensive SCAPS-1D Study

***[1]Abdulrahaman Babajide Ogunji, [2]Taiwo Aiyelero, [2]Adesola Adedokun and [1]Adesanya Oluwafemi Atilade**

[1]Department of Physical Sciences, Lagos State University of Science and Technology, Ikorodu, Lagos, Nigeria
[2]Department of Chemical Sciences Lagos State University of Science and Technology, Ikorodu, Lagos, Nigeria

*Corresponding Author's Email: ogunji.ab@lasustech.edu.ng

ABSTRACT

Non-fullerene organic solar cells based on PM6:ITIC have surpassed 11 % efficiency, but the use of a graphene top anode in inverted architectures remains underexplored in device modelling.This work investigates an inverted organic solar cell with the architecture ITO(cathode)/ZnO/PM6:ITIC/PEDOT:PSS/graphene(anode) using the Solar Cell Capacitance Simulator (SCAPS-1D). The calibration uses two tiers: an ideal low-defect model reproduces the experimental efficiency of PM6:ITIC devices (11.76 %, $J_{sc} = 17.77$ mA cm^{-2}, $V_{oc} = 0.871$ V, $FF = 76.0$ %), while a realistic defect density ($N_t = 2 \times 10^{16}$ cm^{-3}, capture cross-sections = 10^{-19} cm^2) restores a physical thickness optimum. Device optimisation yields an active layer thickness of 200 nm, a ZnO electron transport layer of 30 nm with a donor density of 10^{19} cm^{-3}, and a PEDOT:PSS hole transport layer of 10 nm, to give a final power conversion efficiency of 10.60 % ($J_{sc} = 24.56$ mA cm^{-2}, $V_{oc} = 0.838$ V, $FF = 51.5$ %). The graphene anode work function must exceed 4.4 eV for optimal hole extraction; pristine monolayer graphene (4.5 eV) already lies within the saturation region. Temperature-dependent simulations (280–380 K) reveal a positive voltage coefficient of $+0.50\, mV\, K^{-1}$ characteristic of Shockley–Read–Hall recombination through mid-gap traps. External quantum efficiency spectra show broader photon collection in the optimised device than in the baseline. Taken together, the results yield quantitative design guidelines for graphene-electrode non-fullerene organic solar cells and establish the value of SCAPS-1D as a predictive simulation tool.

Keywords:
Organic solar cells,
PM6:ITIC,
SCAPS-1D simulation,
Graphene electrode,
Non-fullerene acceptor.

INTRODUCTION

The demand for cleaner energy is pushing photovoltaic well beyond silicon (*Green et al., 2021*). Organic solar cells (OSCs) stand out for their flexibility, solution processable, and suitable for roll-to-roll manufacturing (*Hou et al., 2018; Li et al., 2012*). Such properties position OSCs well for building-integrated photovoltaics and portable electronic applications (*Cui et al., 2019*).

Non-fullerene acceptors (NFAs) have reshaped organic photovoltaics by overcoming the fundamental limitations of fullerene-based systems, including weak visible and near-infrared absorption, limited energy level tunability, and poor morphological stability (*Yan et al., 2018; Yuan et al., 2019*). The introduction of ITIC by Zhan and co-workers in 2015 established the first major challenger to fullerene dominance, achieving an initial PCE of 6.80 % with PTB7-Th (*Lin et al., 2015*). Subsequent pairing of ITIC with the wide-bandgap polymer donor PBDB-T pushed efficiencies beyond 11%, with molecular optimisation yielding over 13% (*Zhao et al., 2016; Zhao et al., 2017*). The structurally related polymer donor PM6 (PBDB-T-2F), incorporating fluorine substituents to deepen the HOMO level, has demonstrated PCEs of $10 - 12$ % when combined with ITIC-series acceptors in optimised architectures (Zheng et al., 2020).

Device performance in OSCs depends critically on the charge transport layers and electrode materials. Zinc oxide (ZnO) is a widely validated electron transport layer (ETL) for inverted architectures owing to its wide bandgap ($\sim 3.3\, eV$), high electron mobility, favourable conduction band alignment with NFA acceptors, and compatibility with low-temperature solution processing (*Sun et al., 2011; Hau et al., 2008*). PEDOT: PSS remains the most extensively employed hole transport layer (HTL) due to its high work function, good film-forming properties, and established processing protocols, though its acidic and hygroscopic nature presents long-term stability challenges (*Ouyang, 2013; Hu et al., 2019*).

Conventional OSC architectures rely predominantly on indium tin oxide (ITO) as the transparent electrode. However, indium scarcity, sputtering costs, mechanical brittleness, and degradation from indium diffusion into organic layers motivate the search for alternatives (*Ellmer, 2012; Kumar & Zhou, 2010*). Graphene, a two-dimensional sp^2-hybridised carbon allotrope, has drawn attention as an ITO alternative owing to its high carrier mobility, optical transparency (∼97.7 % per monolayer), outstanding mechanical flexibility, and chemical stability (*Bonaccorso et al., 2015; Bae et al., 2010*). The work function of graphene is also tunable from $\sim 4.2\,eV$ to over $5.0\,eV$ by chemical doping, making it adaptable for use as either a cathode or an anode (*Bonaccorso et al., 2015; Liu et al., 2012*). Device results with graphene electrodes have advanced from early CVD-graphene anodes achieving PCEs comparable to ITO references *(Park et al., 2014*) to flexible graphene-electrode OSCs reaching 15.2 % PCE with polyimide-integrated, p-doped graphene (*Kim et al., 2020*).

Numerical device simulation using SCAPS-1D (Solar Cell Capacitance Simulator in one Dimension), developed at the University of Gent, Belgium, is now a standard methodology for thin-film photovoltaic modelling (*Burgelman et al., 2000; Burgelman et al., 2013*). SCAPS-1D solves the coupled Poisson equation and electron/hole continuity equations under drift-diffusion transport, from which current density–voltage characteristics, quantum efficiency spectra, and energy band diagrams are obtained (*Decock et al., 2011*). The software has been applied to organic solar cell simulation: *Abdelaziz et al.* (2019) demonstrated SCAPS-1D optimisation of PBDB-T: ITIC architectures, achieving 14.25 % simulated PCE; *Nithya and Sudheer (2020)* modelled PBDB-T: ITIC devices with CuI as HTL reaching 15.68 % PCE and expanded to ITIC-OE devices with diverse ETL/HTL candidates (*Nithya & Sudheer, 2022*); *Nowsherwan et al. (2022)* achieved 17.36 % for PBDB-T: ITIC devices with graphene oxide as HTL; and *Muzammil et al. (2024)* reported optimisation of PBDB-T: ITIC systems with WS_2 ETL.

While these studies validated SCAPS-1D for NFA-based OSC simulation, a comprehensive investigation that combines the PM6:ITIC active layer with graphene as the top anode in an inverted ZnO-based architecture, and that explicitly compares ideal and realistically defected models to uncover the physical thickness optimum, has not been reported. How the graphene work function and ZnO doping level jointly govern device behaviour has equally not been examined. The present study fills these gaps with SCAPS-1D simulations, with objectives including: (i) establishing a validated baseline model with ideal and realistic defect parameters; (ii) layer-by-layer thickness optimisation on the realistic device; (iii) defect density tolerance analysis; (iv) ZnO doping optimisation; (v) graphene work function determination and (vi) thermal stability assessment.

MATERIALS AND METHODS

Device Architecture

The inverted organic solar cell consists of the functional elements schematically depicted in Figure 1(a):

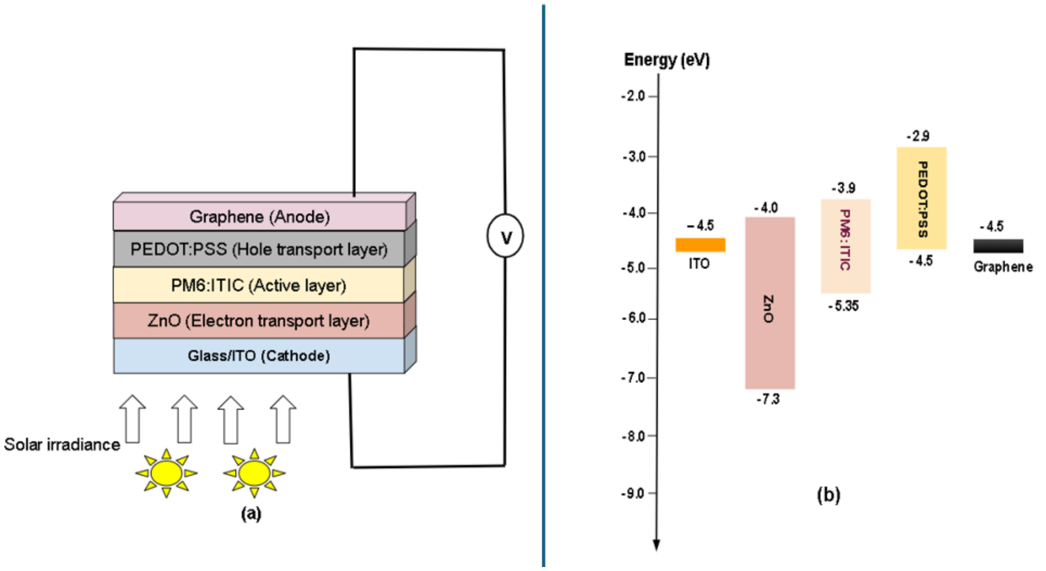

Figure 1: (a) Structural diagram (b). Energy band diagram of ITO/ZnO/PM6:ITIC/PEDOT: PSS /Graphene Organic Solar Cells

Front electrode: A glass substrate coated with indium tin oxide (ITO) serves as the transparent cathode. In SCAPS-1D, the ITO is modelled as a flat-band metal contact with a work function of -4.50 eV.

Electron transport layer (ETL): n-type ZnO with a thickness of 30 nm and a donor doping concentration of 1×10^{19} cm⁻³ (optimised value).

Photoactive layer: A bulk heterojunction of the wide-bandgap polymer donor PM6 and the non-fullerene acceptor ITIC. The optimised thickness is 200 nm.

Hole transport layer (HTL): p-type PEDOT:PSS, 10 nm thick, with an acceptor doping concentration of 1×10^{19} cm⁻³.

Back electrode: Few-layer graphene acts as the top anode. It is defined as a metal contact with a variable work function; the baseline and optimised value is -4.50 eV (pristine monolayer graphene).

The SCAPS-1D simulation treats the ITO and graphene electrodes as metal contacts, not as semiconductor layers. Therefore, the active device stack comprises only the three semiconductor layers: ZnO, PM6:ITIC, and PEDOT: PSS. The layer order, from the illuminated front side to the back, is: ITO (right contact) → ZnO → PM6:ITIC → PEDOT: PSS → Graphene (left contact). Light from an AM 1.5G solar simulator (100 mW cm⁻²) is incident from the ITO side.

Figure 1(b) shows the energy levels of each layer in electron volts (eV) and reveals how charge carriers are selectively extracted after light absorption. Moving from bottom to top electrode: ITO serves as the bottom electrode (work function −4.5 eV). ZnO sits above it as the electron transport layer (ETL), with its conduction band at −4.0 eV and valence band at −7.3 eV, through which electrons are selectively extracted. The PM6:ITIC bulk heterojunction forms the active layer where exciton generation and dissociation occur; its LUMO at −3.9 eV and HOMO at −5.35 eV define the optical gap and sustain charge separation. PEDOT: PSS acts as the hole transport layer (HTL), with its levels spanning −2.9 to −4.5 eV, directing holes toward the top electrode. Graphene completes the stack as the top electrode at −4.5 eV. The modelled PEDOT:PSS valence band (−4.5 eV) lies 0.85 eV above the PM6:ITIC HOMO (−5.35 eV), which would constitute a significant hole-extraction barrier in a full quantum-mechanical treatment. Within the SCAPS-1D drift-diffusion framework, this offset is partially compensated by the high acceptor doping of the HTL (1×10¹⁹ cm⁻³); however, the resulting fill-factor values should be read with this caveat in mind.

The built-in electric field, caused by the work function difference between the n-type ZnO and the p-type PEDOT: PSS, appears as a gentle slope of the bands across the intrinsic PM6:ITIC layer. The equilibrium Fermi level (dashed line in the SCAPS-generated plot) is constant throughout the device.

SCAPS-1D Simulation Framework

Simulations were performed using SCAPS-1D version 3.3.12, developed at the Department of Electronics and Information Systems (ELIS), University of Gent, Belgium (*Burgelman et al., 2000; Burgelman et al., 2013)*. Standard AM 1.5G illumination (100 mW cm⁻²) at 300 K was used for baseline simulations. The software solves the coupled Poisson equation and electron/hole continuity equations under the drift-diffusion model *(Decock et al., 2011).*

The generation rate $G(x)$ is calculated using the SCAPS-1D internal optical model, where each layer is assigned a wavelength-dependent absorption coefficient taken from experimental data of ZnO, PM6:ITIC blends, and PEDOT: PSS. For the active layer, a constant absorption coefficient $\alpha = 8.86 \times 10^4 cm^{-1}$ is used, adjusted to reproduce the experimental short-circuit current density. Reflection losses at the front surface are set to zero (ideal antireflection) to isolate the inherent photovoltaic potential. This assumption overestimates the photon flux entering the device relative to a real ITO-coated glass substrate (typical front-surface reflectance ~of 4–8%) and consequently inflates the simulated Jsc. All efficiency comparisons are therefore made internally between device configurations under identical optical conditions, rather than as absolute experimental benchmarks. Front and back contacts are treated as flat-band metal contacts with surface recombination velocities of $10^7 cms^{-1}$ cm for both carriers.

Governing Equations

The device physics is governed by three coupled equations solved self-consistently:

Poisson's equation – describes how the electrostatic potential within the semiconductor is affected by the distribution of electric charges *(Burgelman et al., 2000; Decock et al., 2011)*

$$\frac{d}{dx}\left(\epsilon(x)\frac{d\psi}{dx}\right) = -q(p(x) - n(x) + N_D^+(x) - N_A^-(x) + other\ charges) \qquad (1)$$

Where $\psi(x)$ is the electrostatic potential at the position x, $\epsilon(x)$ is the position-dependent permittivity, q is elementary charge, $p(x)$ is the hole concentration, $n(x)$ is the electron concentration, $N_D^+(x)$ is the concentration of ionised donors, $N_A^-(x)$ is the concentration of ionized acceptors, and other charges include charges from defects, traps, or interface states. The Poisson's equation ensures that the electric field throughout the device is consistent with the net charge at every point.

Continuity Equations - describe how the populations of electrons and holes change over time due to generation (e.g., by light), recombination, and current flow *(Burgelman et al., 2000; Decock et al., 2011)*.

For electrons:

$$\frac{\partial n}{\partial t} = \frac{1}{q}\frac{\partial J_n}{\partial x} + G_n(x) - R_n(x) \qquad (2a)$$

For holes:

$$\frac{\partial p}{\partial t} = \frac{1}{q}\frac{\partial J_p}{\partial x} + G_p(x) - R_p(x) \qquad (2b)$$

Where n, p are the electron and hole concentrations, J_n, J_p are the electrons and holes current densities, G_n, G_p are the generation rates for electrons and holes, R_n, R_p are the recombination rates for electrons and holes, and t is the time.

Transport Equations (Current Densities)

To solve the continuity equations, SCAPS needs to know how current flows. This is described by the drift-diffusion model *(Burgelman et al., 2000; Decock et al., 2011)*.

Electron Current Density:

$$J_n = q\mu_n nE + qD_n\frac{dn}{dx} \qquad (3a)$$

Hole current Density:

$$J_p = q\mu_p pE - qD_p\frac{dp}{dx} \qquad (3b)$$

Where μ_n, μ_p are the electron and hole mobilities, E is the electric field (E$= \frac{-d\psi}{dx}$), $D_{n,\ p}$ are the electron and hole diffusion coefficients (related to mobility by the Einstein relation:

$$D = \left(\frac{KT}{q}\right)\mu \qquad (4)$$

In effect, current has two drivers:

Drift: charged particles being pulled by the electric field (μnE)

Diffusion: particles moving from areas of high concentration to low concentration ($D\frac{dn}{dx}$).

Shockley-Read-Hall Recombination (Shockley & Read, 1952; Hall, 1952):

$$R_{SRH} = \frac{np - n_i^2}{\tau_p(n+n_1) + \tau_n(p+p_1)} \qquad (5)$$

where n_i is the intrinsic carrier concentration, $\tau_{p,n}$ are carrier lifetimes, and n_1, p_1 are trap-level statistical factors.

Optical Generation Rate:

$$G(x) = \alpha(\lambda) \cdot N_{ph}(\lambda) \cdot exp(-\alpha x) \qquad (6)$$

Performance Metric

Open Circuit Voltage **(V_{oc})**: is the terminal voltage when no external current flows, i.e., the open-circuit condition. *(Burgelman et al., 2000; Green et al., 2021)*

$$V_{oc} = \frac{KT}{q}\ln\left(\frac{I_{ph}}{I_0} + 1\right) \qquad (7)$$

K is Boltzmann's constant = 1.380649 × 10^{-23} m^2 kg s^{-2} K^{-1}

T is the temperature of the solar cell measured in Kelvin

I_{ph} is the photocurrent (i.e., the current generated by absorbed light)

I_0 is the saturation current (i.e., the reverse leakage current under normal illumination)

Fill factor (FF)*:* is a central parameter in characterising solar cell performance or photovoltaic (PV) device. The fill factor is defined as:

$$FF = \frac{V_m \cdot J_m}{V_{oc} \cdot J_{sc}} \qquad (8)$$

Where

V_m is the voltage at the maximum power point (i.e., the voltage at which the solar cell generates the maximum power).

J_m is the current at the maximum power point (i.e., the current at which the solar cell generates the maximum power).

Power Conversion Efficiency (PCE)*:* is the primary figure of merit for photovoltaic devices and is defined as:

$$PCE = \frac{(P_{max})}{(P_{in})} \times 100\% = \frac{J_{sc} \times V_{oc} \times FF \times A}{P_{in}} \qquad (9)$$

Where P_{max} is the maximum power output, Pin is the incident solar power density (typically 100 mWcm-² under AM1.5G conditions), A is the area of the solar cell, J_{sc} is the short-circuit current density, V_{oc} is the open-circuit voltage, and FF is the fill factor *(Burgelman et al., 2013)*.

Short Circuit Current Density (J_{sc}): is the maximum extractable current, bounded by the photon flux and the device's absorption characteristics *(Burgelman et al., 2013)*:

$$J_{sc} = \frac{q}{A}\int_0^\infty \frac{G(\lambda) \cdot \eta(\lambda)}{h \cdot c}\, dA \qquad (10)$$

Where

q is the electron charge $q = 1.602 \times 10^{-19}C$,

$G(\lambda)$ is the spectral irradiance at wavelength (λ) which represents the amount of light energy that reaches the solar cell at that wavelength,

$\eta(\lambda)$ is the quantum efficiency of the solar cell at wavelength (λ), which indicates how effectively photons of that wavelength are converted into electrical carriers.

h is Planck's constant $6.626 \times 10^{-34} J.s$,

c is the speed of the light $3.0 \times 10^8 ms^{-1}$

In many practical applications, especially under standard test conditions (STC), J_{sc} can also be approximated by the following simpler expression:

$$J_{sc} = \frac{q}{A}\int_0^\infty G(\lambda) \cdot \eta(\lambda) dA \qquad (11)$$

Material Parameters

The baseline parameters for the three active layers are listed in Table 1. These values are taken from experimental reports *(Zhao et al., 2016; Zhao et al., 2017; Zheng et al., 2020)* and validated SCAPS-1D studies on non-fullerene acceptor solar cells *(Abdelaziz et al., 2019; Nithya & Sudheer, 2020; Nithya & Sudheer, 2022; Nowsherwan et al., 2022; Muzammil et al., 2024).*

Table 1: Material parameters for the three active layers used in the SCAPS-1D simulation. ITO and graphene electrodes are defined as metal contacts with work functions of 4.50 eV (baseline)

Parameter	ZnO (ETL)	PM6:ITIC (Active)	PEDOT:PSS (HTL)
Thickness (nm)	50	100	10
Bandgap E_g (eV)	3.3	1.45	1.6
Electron affinity χ (eV)	4.0	3.9	2.9
Relative permittivity ε_r	9.0	3.9	3.0
CB effective density of states N_C (cm⁻³)	2.2×10^{18}	1.0×10^{21}	2.2×10^{18}
VB effective density of states N_V (cm⁻³)	1.8×10^{19}	1.0×10^{21}	1.8×10^{19}
Electron mobility μ_n (cm² V⁻¹ s⁻¹)	100	4.5×10^{-4}	4.5×10^{-5}
Hole mobility μ_p (cm² V⁻¹ s⁻¹)	25	4.5×10^{-4}	4.5×10^{-5}
Shallow donor density N_D (cm⁻³)	1×10^{19}	0	0
Shallow acceptor density N_A (cm⁻³)	0	0	1×10^{19}
Bulk defect properties			
Defect type	Neutral	Neutral	Neutral
Total density N_t (cm⁻³)	1×10^{15}	1×10^{12} (ideal) / 2×10^{16} (realistic)	1×10^{15}
Energy level	mid-gap (1.65 eV above E_V)	mid-gap (0.725 eV above E_V)	mid-gap (0.80 eV above E_V)
Capture cross-sections (cm²)	1×10^{-14}	1×10^{-19}	1×10^{-14}
Characteristic energy (eV)	0.1	0.1	0.1
References	*(Sun et al., 2011; Hau et al., 2008; Abdelaziz et al., 2019; Nithya & Sudheer, 2020)*	*(Zhao et al., 2016; Zhao et al., 2017; Zheng et al., 2020; Abdelaziz et al., 2019; Nithya & Sudheer, 2020; Nowsherwan et al., 2022)*	*(Ouyang, 2013; Hu et al., 2019; Abdelaziz et al., 2019; Nithya & Sudheer, 2020; Nowsherwan et al., 2022)*

The ZnO electron mobility of 100 cm² V⁻¹ s⁻¹ represents an upper-bound value consistent with high-crystallinity ZnO films; solution-processed nanoparticle ZnO typically yields 1–10 cm² V⁻¹ s⁻¹, and the near-zero series-resistance conclusion of Section 3.3.1 should be interpreted within this idealisation.

Contact definitions (baseline)

Front contact (ITO cathode): Work function = 4.50 eV, surface recombination velocity = 10^7 cm s⁻¹.

Back contact (Graphene anode): Work function = 4.50 eV (pristine monolayer), surface recombination velocity = 10^7 cm s⁻¹.

Interface Properties

Two internal interfaces are defined: ZnO/PM6:ITIC and PM6:ITIC/PEDOT: PSS. In the baseline, each interface is assigned a neutral Gaussian-distributed defect density of 10^{10} cm⁻² centred at the mid-gap, with capture cross-sections of $10^{-14}\mathrm{cm}^2$.

Simulation Procedure

The work proceeded in two stages: device optimisation followed by supporting physical analyses to interpret the results. All simulations used AM 1.5G illumination ($100\ mW\ cm^{-2}$) at 300 K except where noted.

These optimisation sweeps all used the realistic device (PM6:ITIC $N_t = 2 \times 10^{16}\ \mathrm{cm}^{-3}$, $\sigma = 10^{-19}\mathrm{cm}^2$), which was first calibrated against the ideal low-defect baseline. The sequence is summarised in Table 2.

Table 2: Sequential device optimisation workflow

Step	Parameter varied	Range	Fixed layers/notes
1	PM6:ITIC thickness	50–250 nm	Baseline ZnO 50 nm; ideal N_t for calibration, then switched to realistic N_t for optimization
2	ZnO thickness	10–100 nm	PM6:ITIC at optimised 200 nm
3	PEDOT: PSS thickness	5–50 nm	PM6:ITIC 200 nm, ZnO 30 nm
4	ZnO donor density N_D	10^{16}–10^{20} cm^{-3}	PM6:ITIC 200 nm, ZnO 30 nm, PEDOT: PSS 10 nm
5	Temperature	280–380 K	Optimised device (ZnO 30 nm, active 200 nm, ZnO doping 10^{19} cm^{-3})
6	Graphene work function	4.0–5.5 eV	Same optimised device

RESULTS AND DISCUSSION

Ideal Baseline and Realistic Calibration

As a starting point for device optimisation, two baseline models were built that differ only in the bulk defect density of the PM6:ITIC active layer. The corresponding current density–voltage characteristics are shown in Figure 2, and the photovoltaic parameters are listed in Table 3a.

The ideal baseline ($N_t = 1 \times 10^{12} cm^{-3}$, $\sigma = 1 \times 10^{-19} cm^2$) yields a power conversion efficiency of 11.76 % ($V_{oc} = 0.871V$, $J_{sc} = 17.77\ mAcm^{-2}$, $FF = 76.0\ \%$). This value falls within the $10 - 12\ \%$ range reported for experimental PM6:ITIC devices *(Zhao et al., 2016; Zheng et al., 2020)*, which supports the choice of material parameters. However, owing to negligible Shockley–Read–Hall (SRH) recombination, the efficiency of the ideal model increases monotonically with active-layer thickness and does not exhibit a maximum; such behaviour is not observed in real bulk-heterojunction cells, where recombination losses ultimately limit the usable thickness.

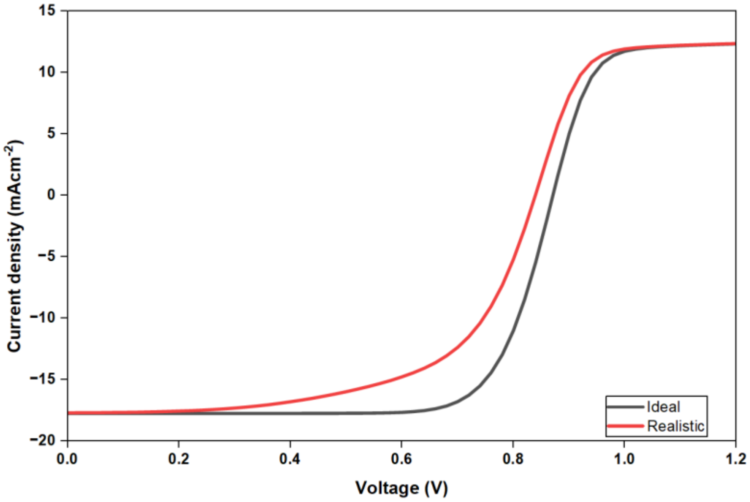

Figure 2: Illuminated current density–voltage (J–V) characteristics of the (a) ideal $N_t = 1 \times 10^{12} cm^{-3}$ and (b) realistic $N_t = 2 \times 10^{16} cm^{-3}$baseline devices (active layer thickness = 100 nm)

Physically meaningful recombination was introduced by setting the bulk defect density to realistic baseline was constructed by increasing the bulk defect density to $N_t = 2 \times 10^{16} cm^{-3}$, consistent with trap concentrations reported for solution-processed organic blends *(Shockley & Read, 1952; Hall, 1952)*. All other parameters remained identical to the ideal model. The realistic device achieves an efficiency of 9.01 % ($V_{oc} = 0.839\ V$, $J_{sc} = 17.71 mAcm^{-2}$, FF =60.6 %). The short-circuit current is practically unchanged, which shows that photogeneration is insensitive to defect density. The 2.75 percentage-point drop in efficiency relative to the ideal case arises predominantly from a reduction in fill factor ($\Delta FF = -15.4$ percentage points) driven by enhanced bulk SRH recombination, with a smaller contribution from the voltage loss ($\Delta V_{oc} = -32\ mV$).

Table 3a: Photovoltaic parameters of the ideal and realistic baseline devices (active layer thickness = 100 nm)

Model	V_{oc} (V)	J_{sc} ($mA\,cm^{-2}$)	FF (%)	PCE (%)
Ideal ($N_t = 10^{12}$ cm^{-3})	0.871	17.77	76.0	11.76
Realistic ($N_t = 2 \times 10^{16}$ cm^{-3})	0.839	17.71	60.6	9.01

The realistic baseline thus provides a suitable starting point for the subsequent optimisation: it preserves an efficiency level that is experimentally plausible while introducing a recombination strength sufficient to produce a physically meaningful thickness optimum. All optimisation sweeps described in Sections 3.2–3.7 were performed on this realistic device. The choice of $N_t = 2 \times 10^{16} cm^{-3}$ as the realistic calibration point, the bulk defect density of the PM6:ITIC layer was swept from $1 \times 10^{12} cm^{-3}$ to $1 \times 10^{17} cm^{-3}$ cm^{-3} while all other parameters were held at the baseline values (active layer 100 nm). Six representative points are listed in Table 3b; the complete 17-point dataset is provided in Table S1 of the Supplementary Information.

Across the full range, Jsc remains essentially constant at $\approx 17.7 - 19.1\, mAcm^{-2}$, indicating that photogeneration is independent of trap density. The open-circuit voltage holds above $0.86\,V$ for $N_t \leq 1 \times 10^{16} cm^{-3}$, then decreases sharply to $0.78\,V$ at $1 \times 10^{17} cm^{-3}$ as SRH recombination increasingly dominates. The fill factor is the most sensitive parameter, declining monotonically from 76.0 % at the ideal limit to 40.8 % at $1 \times 10^{17} cm^{-3}$. Consequently, PCE falls from 11.76 % to 6.02 % over this range.

Table 3b: Representative defect density tolerance data for the PM6:ITIC active layer (thickness = 100 nm, all other parameters at their baseline values)

$N_t (cm^{-3})$	V_{oc} (V)	J_{sc} ($mA\,cm^{-2}$)	FF (%)	PCE (%)
1×10^{12} (ideal)	0.871	17.77	76.0	11.76
1×10^{15}	0.87	19.1	74.87	12.48
1×10^{16}	0.86	19.07	67.14	10.90
2×10^{16} (adopted)	0.839	17.71	60.6	9.01
5×10^{16}	0.81	18.95	49.07	7.57
1×10^{17}	0.78	18.8	40.8	6.02

The value $2 \times 10^{16} cm^{-3}$ was selected because it simultaneously satisfies two physical criteria: (i) it reproduces the experimentally reported PCE range of $9 - 10$ % for non-optimised PM6:ITIC devices *(Zhao et al., 2016; Zheng et al., 2020)*, yielding $\eta = 9.01$ % here; and (ii) it introduces sufficient SRH recombination to produce the physically meaningful thickness optimum examined presented in the following subsection. Defect densities below $5 \times 10^{15} cm^{-3}$ maintain PCE above 11.75 %, inconsistent with un-optimised experimental devices, while densities at or above $1 \times 10^{17}\, cm^{-3}$ collapse the fill factor below 41 % and the PCE to 6.02 %, significantly overestimating recombination losses. This value is the most physically consistent calibration point within the experimentally plausible window.

Active-Layer Thickness Optimisation

The PM6:ITIC layer thickness in the realistic device ($N_t = 2 \times 10^{16}\ cm^{-3}$) was swept from 50 nm to 250 nm in thirteen steps; all other layer parameters were held at the values established in the calibration in the Ideal Baseline and Realistic Calibration section. The extracted photovoltaic parameters are shown in Figure 3, and representative values are listed in Table 4.

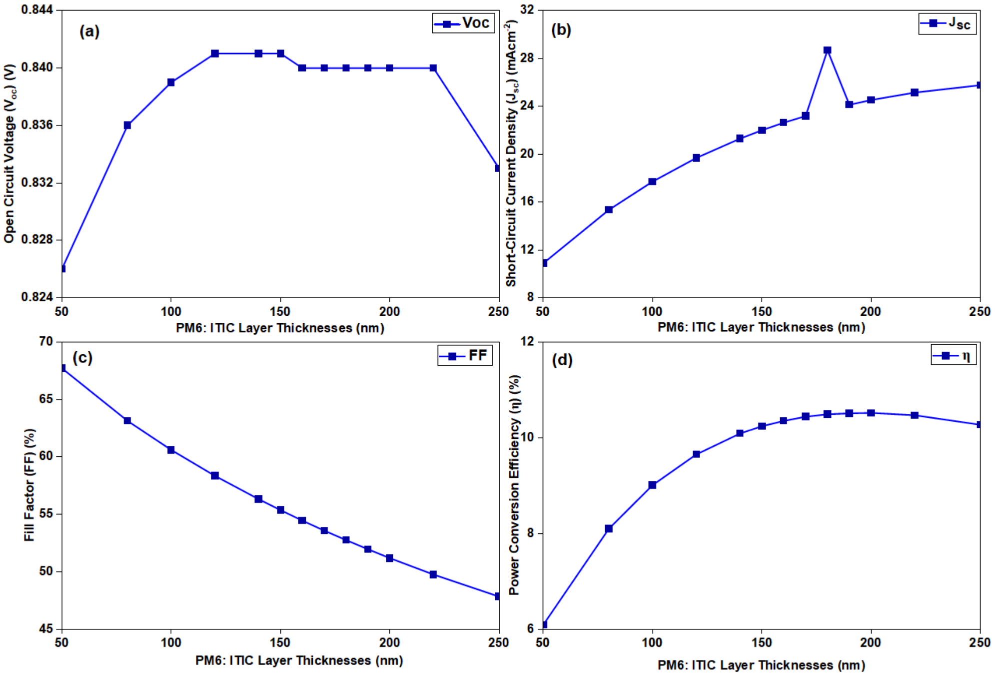

Figure 3: Photovoltaic parameters as a function of PM6:ITIC active layer thickness for the realistic device ($N_t = 2 \times 10^{16}$ cm⁻³). (a) V_{oc} (b) J_{sc} (c)FF and (d) PCE

J_{sc} rises monotonically from $10.88\ mA\ cm^{-2}$ at 50 nm to $25.77\ mA\ cm^{-2}$ at 250 nm, as the longer optical path captures more photons. The fill factor exhibits the opposite trend, decreasing from 67.7 % to 47.8 % because the longer average drift distance amplifies bulk Shockley–Read–Hall recombination. The open-circuit voltage remains nearly constant between 100 nm and 220 nm $(0.839 - 0.841\ V)$ and drops by only 7 mV at 250 nm, showing that the built-in field is largely preserved across the investigated range.

The power conversion efficiency reaches a well-defined maximum of 10.52 % at a thickness of 200 nm (Table 4). This corresponds to an absolute improvement of 1.51 percentage points, or a relative gain of 16.8 %, over the realistic baseline of 9.01 % at 100 nm. The existence of a peak—absent in the ideal model- arises because the realistic defect density imposes a trade-off between optical absorption and charge-carrier recombination. For comparison, *Abdelaziz et al. (2019)* reported an optimum absorber thickness of approximately 120 nm for a PBDB-T:ITIC device modelled with a lower defect density, and *Nowsherwan et al. (2022)* obtained optimum thicknesses in the 100–150 nm range for a similar system. The larger optimum of 200 nm found here stems from two concurrent factors: the use of PM6, whose hole mobility is lower than that of PBDB-T, and the intentionally elevated bulk trap density, which suppresses the fill factor more rapidly beyond the optimum, thereby shifting the peak to greater thicknesses.

One data point at 180 nm exhibited an anomalously high Jsc of 28.69 mA cm⁻², incompatible with the otherwise smooth absorption-limited trend. The simulation was re-run at this thickness with tightened convergence tolerances and a finer spatial mesh; the anomaly persisted, pointing to a numerical instability in the SCAPS-1D solver at this specific combination of defect density and layer thickness rather than a physical trend. This point is excluded from the optimum determination; the complete 13-point dataset including the flagged value is provided in the Supplementary Information.

Table 4: Selected photovoltaic parameters from the active-layer thickness sweep on the realistic device ($N_t = 2 \times 10^{16}$ cm⁻³). The complete 13-point dataset is available in the Table S2 of the Supplementary Information

Thickness (nm)	V_{oc} (V)	J_{sc} (mA cm⁻²)	*FF* (%)	PCE (%)
50	0.826	10.88	67.71	6.09
100	0.839	17.71	60.60	9.01
150	0.841	22.00	55.36	10.24
200	**0.840**	**24.53**	**51.19**	**10.52**
220	0.840	25.15	49.76	10.47
250	0.833	25.77	47.83	10.27

The optimised active-layer thickness of 200 nm is fixed for all subsequent optimisation steps (ZnO ETL thickness and doping, temperature dependence, and graphene work function).

ZnO Electron Transport Layer: Thickness and Doping Optimisation

The ZnO ETL was optimised in two sequential steps. First, the layer thickness was varied while the donor density was held at $N_D = 1 \times 10^{18}$ cm⁻³. Second, with the thickness fixed at its optimum value, the donor density was swept.

Thickness Optimisation

With the active layer at 200 nm and all other parameters unchanged, the ZnO thickness was varied from 10 nm to 100 nm. The extracted parameters are listed in Table 5 and plotted in Figure 4. The device shows an exceptionally weak dependence on ZnO thickness. J_{sc} remains virtually constant at $\approx 24.5\ mA\ cm^{-2}$, declining by only $0.2\ mA\ cm^{-2}$ between 30 nm and 100 nm. The fill factor increases by 0.2 percentage points between 10 nm and 30 nm and then plateaus at ≈51.2 %. The open-circuit voltage is unchanged at 0.838 V. Consequently, the PCE peaks at 10.52 % at 30 nm, and remains within 0.04 percentage points of this value up to 50 nm. Below 20 nm a slight decrease (10.48 %) suggests incomplete film coverage; above 60 nm a marginal decline reflects weak ultraviolet absorption in ZnO.

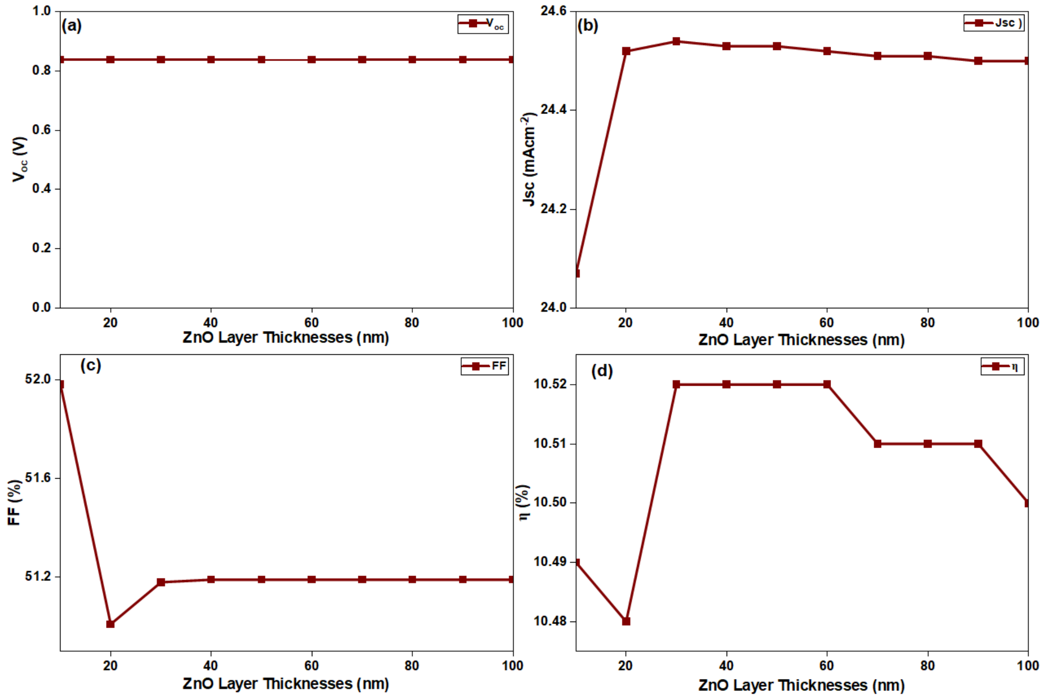

Figure 4: Influence of ZnO ETL thickness on device performance (active layer fixed at 200 nm, $N_D = 1 \times 10^{18}$ cm⁻³). (a) V_{oc} (b) J_{sc} (c)FF and (d) PCE

This flat response is in line with prior SCAPS studies on inverted non-fullerene devices *(Abdelaziz et al., 2019; Nowsherwan et al., 2022)* and follows from the device physics: the high electron mobility of ZnO (100 cm² V⁻¹ s⁻¹ in the present model) makes series resistance negligible once a continuous film is formed, and the favourable conduction-band offset (0.1 eV) ensures ohmic electron extraction *(Sun et al., 2011).*

Table 5: Photovoltaic parameters as a function of ZnO thickness (active layer = 200 nm, $\mathbf{N_D = 1 \times 10^{18}}$ cm⁻³, $\mathbf{N_t = 2 \times 10^{16}}$ cm⁻³)

ZnO thickness (nm)	V_{oc} (V)	J_{sc} (mA cm⁻²)	FF (%)	PCE (%)
10	0.838	24.07	51.98	10.49
20	0.838	24.52	51.01	10.48
30	**0.838**	**24.54**	**51.18**	**10.52**
50	0.838	24.53	51.19	10.52
100	0.838	24.50	51.19	10.50

A thickness of **30 nm** was adopted for the subsequent doping optimisation.

Donor Density Optimisation

With the ZnO thickness fixed at 30 nm, the shallow donor concentration N_D was varied from 1×10^{16} cm⁻³ to 1×10^{20} cm⁻³ (Table 6, Figure 5).

V_{oc} remains constant at 0.838 V across the entire range, showing that the built-in potential is already fully developed at the lowest doping. J_{sc} rises marginally from 23.91 mA cm⁻² at 10^{16} cm⁻³ to 24.57 mA cm⁻² at 10^{20} cm⁻³, while FF decreases from 51.67 % to 51.58 %, consistent with negligible changes in recombination dynamics across this doping range.

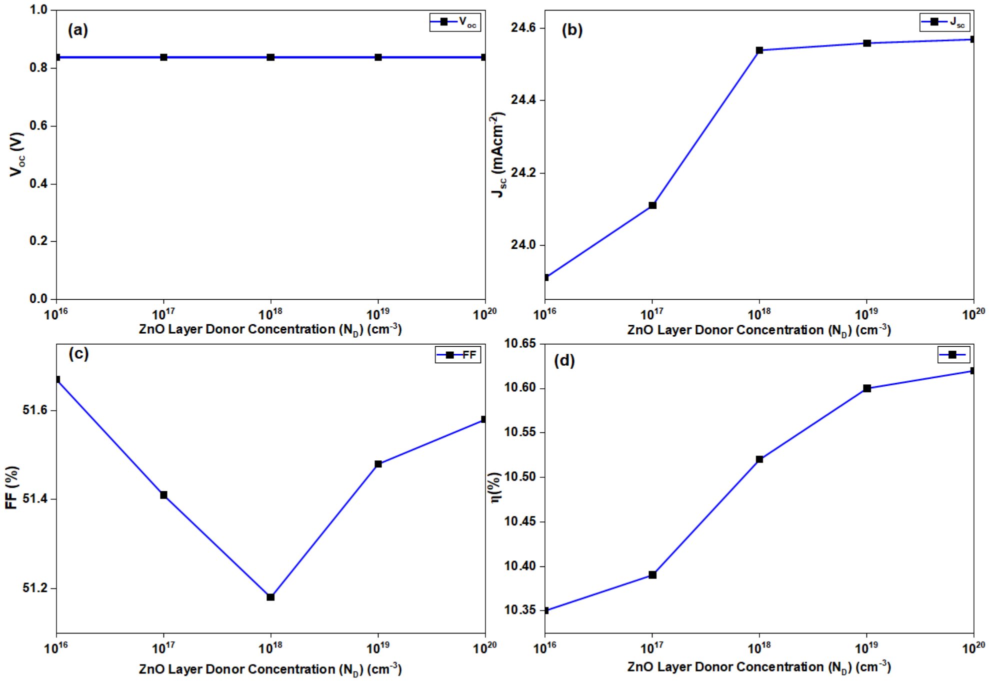

Figure 5: ZnO donor doping concentration sweep. PCE saturates beyond $1 \times 10^{19}\ cm^{-3}$. (a) V_{oc} (b) J_{sc} (c)FF and (d) PCE

The PCE improves from 10.35 % at the lowest doping to **10.62 %** at $N_D = 1 \times 10^{20}$ cm⁻³, with 99.8 % of the total improvement already achieved at $N_D = 1 \times 10^{19}$ cm⁻³ (η = 10.60 %).

Saturation of this kind is expected for doped transport layers: once the donor concentration reaches the point to form an ohmic contact, further increases yield negligible benefit *(Sun et al., 2011)*. The observed optimum range of 10^{18}–10^{19} cm⁻³ is consistent with previous SCAPS-1D studies on ZnO-based ETLs *(Abdelaziz et al., 2019; Nowsherwan et al., 2022)* and with experimental doping levels of solution-processed ZnO films.

Table 6: Photovoltaic parameters as a function of ZnO donor density (ZnO thickness = 30 nm, active layer = 200 nm, $N_t = 2 \times 10^{16}$ cm⁻³)

N_D (cm⁻³)	V_{oc} (V)	J_{sc} (mA cm⁻²)	FF (%)	PCE (%)
1×10^{16}	0.838	23.91	51.67	10.35
1×10^{17}	0.838	24.11	51.41	10.39
1×10^{18}	0.838	24.54	51.18	10.52
1×10^{19}	**0.838**	**24.56**	**51.48**	**10.60**
1×10^{20}	0.838	24.57	51.58	10.62

The PCE reaches its maximum of 10.60 % at $ND = 1 \times 10^{19}\, cm^{-3}$, with only a negligible further gain of 0.02 percentage points at $1 \times 10^{20}\, cm^{-3}$. Given that $1 \times 10^{19}\, cm^{-3}$ captures near-maximum efficiency and represents an experimentally accessible doping level for solution-processed ZnO, this concentration is adopted as the final device parameter, yielding a final PCE of 10.60 % ($J_{sc} = 24.56\, mA\, cm^{-2}$, $V_{oc} = 0.838V$, FF = 51.5 %).

Summary of ZnO Optimisation

The optimised ZnO ETL has a thickness of 30 nm and a donor density of 1×10^{19} cm⁻³. With these parameters the device PCE is 10.60 %, representing an additional gain of 0.08 percentage points over the thickness-only optimisation. Because this doping level captures the near-maximum efficiency and is well within the values reported for solution-processed ZnO, it is adopted for the final device. Temperature dependence, HTL thickness, and graphene work function sweeps all used $N_D = 1 \times 10^{19}$ cm⁻³.

Temperature Dependence

The fully optimised realistic device (active layer 200 nm, ZnO 30 nm, $N_D = 1 \times 10^{19}$ cm⁻³, $N_t = 2 \times 10^{16}$ cm⁻³) was simulated from 280 K to 380 K under AM 1.5G illumination. The extracted parameters are listed in Table 7 and shown in Figure 6.

The short-circuit current density is nearly temperature-independent, decreasing only from 24.56 mA cm⁻² at 300 K to 24.43 mA cm⁻² at 380 K. The open-circuit voltage exhibits a positive temperature coefficient: between 280 K and 320 K, V_{oc} rises from 0.828 V to 0.848 V, corresponding to +0.50 mV K⁻¹. This behaviour is characteristic of Shockley–Read–Hall recombination through mid-gap traps (Shockley & Read, 1952; Hall, 1952): as temperature increases, the trap occupancy shifts in such a way that the effective recombination lifetime *increases*, allowing a larger quasi-Fermi level splitting. It should be noted that this positive temperature coefficient is specific to the mid-gap trap parameters used in the SCAPS-1D model; its occurrence in real PM6:ITIC devices would require experimental confirmation via temperature-dependent J–V measurements, as standard organic solar cells more commonly exhibit a negative V_{oc} temperature coefficient governed by dark saturation current.

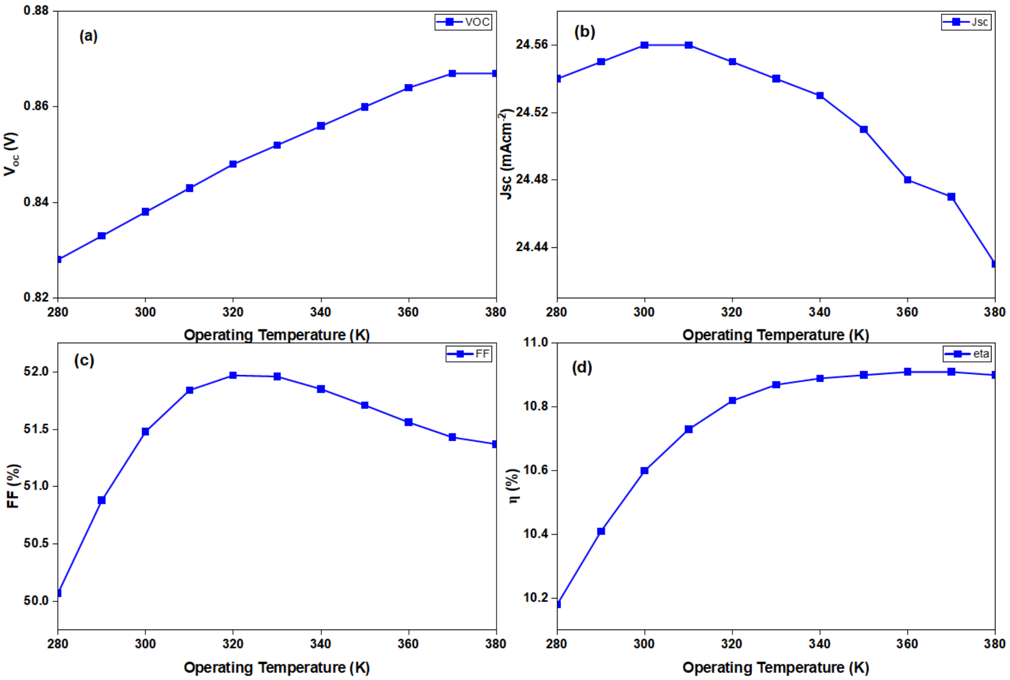

Figure 6: Temperature dependence of the photovoltaic parameters for the fully optimised realistic device. (a) V_{oc} (b) J_{sc} (c)FF and (d) PCE

The fill factor increases from 50.07 % at 280 K to a maximum of 51.97 % at 320 K, then declines gradually to 51.37 % at 380 K. The PCE follows the combined trend, rising from 10.18 % at 280 K to a broad maximum of 10.91 % at 360–370 K, and settling at 10.90 % at 380 K. Over the operating range 300–340 K, the PCE remains above 10.6 % and varies by less than 0.3 percentage points, pointing to good thermal stability.

Table 7: Temperature-dependent photovoltaic parameters of the final optimised realistic device

Temperature (K)	V_{oc} (V)	J_{sc} (mA cm^{-2})	FF (%)	PCE (%)
280	0.828	24.54	50.07	10.18
290	0.833	24.55	50.88	10.41
300	0.838	24.56	51.48	10.6
310	0.843	24.56	51.84	10.73
320	0.848	24.55	51.97	10.82
330	0.852	24.54	51.96	10.87
340	0.856	24.53	51.85	10.89
350	0.860	24.51	51.71	10.90
360	0.864	24.48	51.56	10.91
370	0.867	24.47	51.43	10.91
380	0.867	24.43	51.37	10.90

The next section maps how the graphene anode work function shapes device performance and identifies the minimum work function needed for efficient hole extraction.

PEDOT:PSS Hole Transport Layer Thickness

With the ZnO ETL fixed at 30 nm and $N_D = 1 \times 10^{19}$ cm⁻³, and the active layer at 200 nm ($N_t = 2 \times 10^{16}$ cm⁻³), the PEDOT:PSS thickness was varied from 5 nm to 50 nm. The resulting parameters are listed in Table 8 and plotted in Figure 7.

Table 8: Photovoltaic parameters as a function of PEDOT:PSS thickness (optimised device)

HTL thickness (nm)	V_{oc} (V)	J_{sc} (mA cm⁻²)	FF (%)	PCE (%)
5	0.838	24.56	51.50	10.60
10	0.838	24.56	51.48	10.60
20	0.838	24.56	51.48	10.59
30	0.838	24.56	51.44	10.59
40	0.838	24.56	51.42	10.59
50	0.838	24.56	51.40	10.58

HTL thickness has no measurable effect on device performance. The open-circuit voltage remains constant at 0.838 V, the short-circuit current density at 24.56 mA cm⁻², and the fill factor between 51.40 % and 51.50 %, yielding a PCE of 10.58–10.60 %. The slight decrease at the largest thicknesses is negligible. This outcome agrees with earlier reports on PEDOT:PSS in inverted organic solar cells *(Ouyang, 2013),* and the standard thickness of 10 nm is retained.

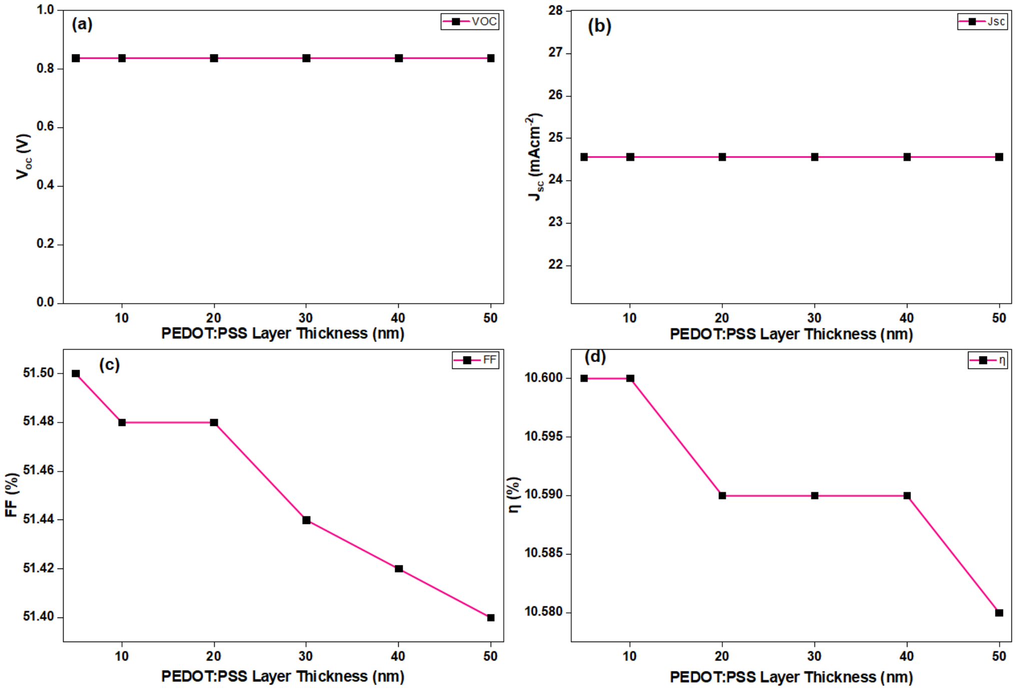

Figure 7: Photovoltaic parameters as a function of PEDOT:PSS hole transport layer thickness for the realistic device ($N_t = 2 \times 10^{16}$ cm⁻³). (a) V_{oc} (b) J_{sc} (c)FF and (d) PCE

Graphene Work Function Dependence

The back-contact work function was swept from 4.0 eV to 5.5 eV on the device with ZnO thickness 30 nm, active layer 200 nm, ZnO doping 1×10^{19} cm⁻³, and realistic defects ($N_t = 2 \times 10^{16}$ cm⁻³). Figure 8 shows the resulting parameters, and Table 9 lists the values.

Below 4.4 eV, a hole-extraction barrier forms, collapsing V_{oc} and FF; at 4.0 eV the PCE drops to 6.31 %. Above 4.4 eV, the performance saturates completely: PCE remains constant at 10.60 % up to 5.5 eV. The open-circuit voltage stabilises at 0.838 V and the fill factor at ≈51.5 %.

Pristine monolayer graphene (4.4–4.5 eV) therefore already lies within the saturation region (Liu et al., 2012). Mild p-doping (e.g., HNO_3 or $AuCl_3$ treatment to 4.7–5.0 eV) provides a safe processing margin without affecting efficiency *(Bonaccorso et al., 2015; Park et al., 2014)*. Heavy chemical modification of the graphene anode is therefore not required.

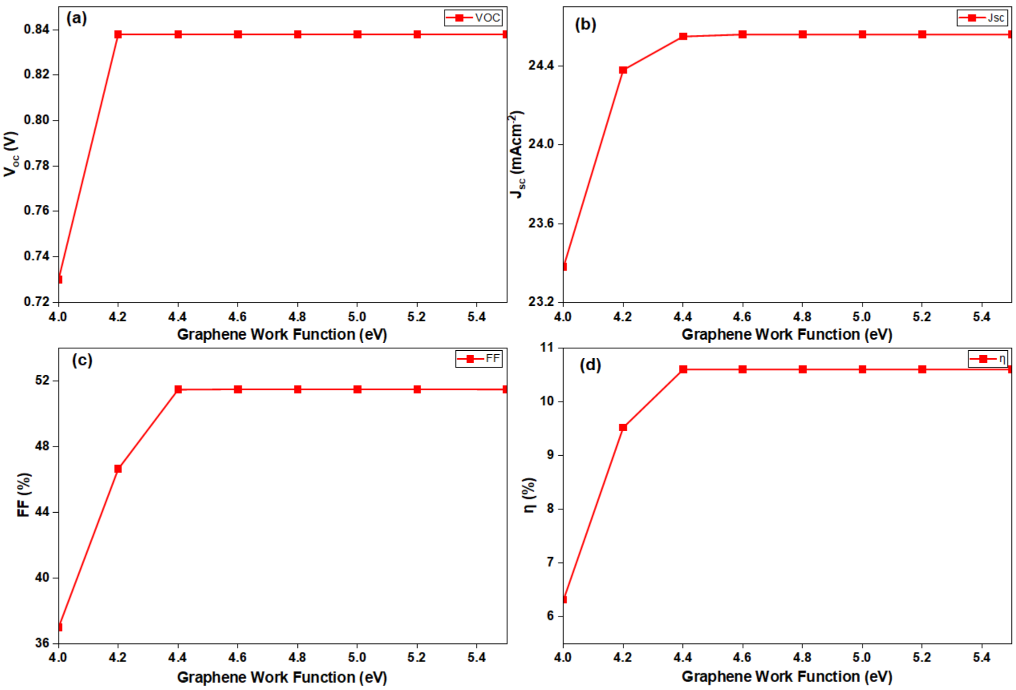

Figure 8: Effect of graphene anode work function on device performance. Performance saturates for work functions ≥ 4.4 eV. (a) V_{oc} (b) J_{sc} (c)FF and (d) PCE

Table 9: Influence of graphene anode work function on device performance

Work function (eV)	V_{oc} (V)	J_{sc} (mA cm^{-2})	FF (%)	PCE (%)
4	0.73	23.38	36.97	6.31
4.2	0.838	24.38	46.63	9.52
4.4	0.838	24.55	51.47	10.6
4.6	0.838	24.56	51.49	10.6
4.8	0.838	24.56	51.49	10.6
5	0.838	24.56	51.49	10.6
5.2	0.838	24.56	51.49	10.6
5.5	0.838	24.56	51.48	10.6

External Quantum Efficiency

The external quantum efficiency (EQE) of the realistic baseline (active layer 100 nm) and the fully optimised device (active layer 200 nm) was calculated under short-circuit, AM 1.5G illumination. The resulting spectra are shown in Figure 9. The increased EQE of the optimised device reflects the enhanced absorption due to the thicker active layer.

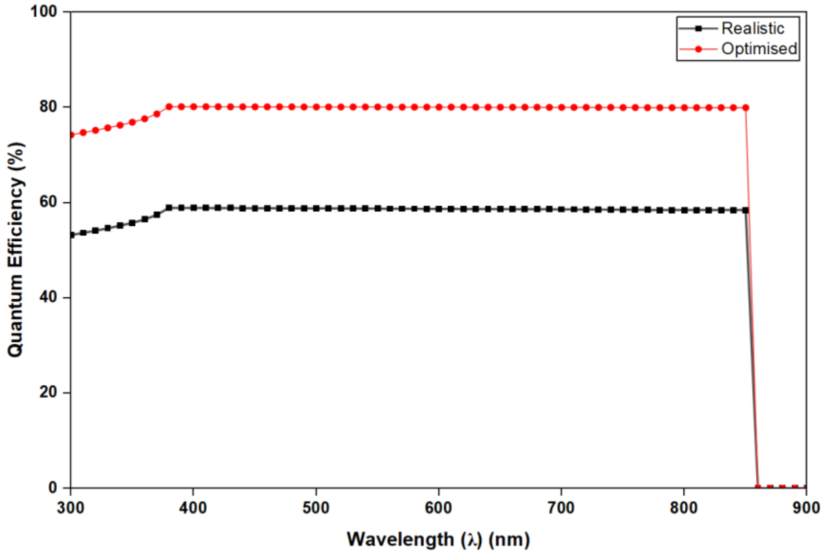

Figure 9: External quantum efficiency (EQE) of the realistic baseline (100 nm) and the fully optimised device (200 nm). The increased EQE of the optimised device reflects the enhanced absorption due to the thicker active layer

Both devices exhibit broad photo-response from 300 nm to 900 nm, with a plateau across the visible region. The baseline device reaches a maximum EQE of approximately 60 %, while the optimised device attains ≈ 80 % across the same range. The higher EQE of the optimised device reflects the increased optical path length of the 200 nm active layer, which absorbs a larger fraction of the incident photons. The integrated J_{sc} values derived from the EQE spectra are consistent with the current densities extracted from the J–V curves (17.71 mA cm^{-2} for the baseline and 24.56 mA cm^{-2} for the optimised device), in good agreement with the J–V results and attesting to the internal consistency of the optical model.

The flat spectral profile follows from the constant absorption coefficient assumed in the simulations; a wavelength-dependent absorption file would reproduce the specific absorption features of the PM6:ITIC blend, but the comparative trend—greater EQE with a thicker absorber—holds regardless.

CONCLUSION

A realistic defect density of 2×10^{16} cm^{-3} is necessary to reproduce the thickness optimum in PM6:ITIC solar cells. The ideal low-defect model achieves 11.76 % but lacks a physical maximum, whereas the realistic model reproduces behaviour seen in experiment. Optimisation yielded an active layer of 200 nm, a ZnO ETL of 30 nm doped at 10^{19} cm^{-3}, and a PEDOT:PSS HTL of 10 nm, giving a final efficiency of 10.60 % – a relative improvement of 17.6 % over the realistic baseline. The ZnO thickness has a negligible influence once a continuous film is formed, and the HTL thickness is entirely without effect, pointing to wide fabrication tolerances. The positive temperature coefficient of V_{oc} $(+0.50\, mV\, K^{-1})$ and the saturation of the graphene work function above 4.4 eV are each consistent with an SRH-dominated recombination regime and support the use of pristine or lightly doped graphene as the anode. The external quantum efficiency of the optimised device reaches ≈ 80 % across the visible region, reflecting the broader photon absorption achieved with the thicker absorber. Collectively, these findings offer quantitative design guidelines for flexible, indium-free organic solar cells and illustrate how defect-aware SCAPS-1D simulation can guide predictive device optimisation. Further gains may be explored through ETL bandgap engineering (e.g., $Zn_{1-x}Mg_xO$ alloys), alternative HTLs with higher work functions, and morphology-aware transport models.

ACKNOWLEDGEMENTS

The authors gratefully acknowledge Prof. Marc Burgelman and the ELIS group, University of Gent, Belgium, for providing SCAPS-1D.

REFERENCES

Abdelaziz, W., Shaker, A., Abouelatta, M., & Zekry, A. (2019). Possible efficiency boosting of a non-fullerene acceptor solar cell using device simulation. *Optical Materials, 91*, 239–245.

Bae, S., Kim, H., Lee, Y., Xu, X., Park, J.-S., Zheng, Y., … & Iijima, S. (2010). Roll to roll production of 30 inch graphene films for transparent electrodes. *Nature Nanotechnology, 5*(8), 574–578.

Bonaccorso, F., Colombo, L., Yu, G., Stoller, M., Tozzini, V., Ferrari, A. C., … & Pellegrini, V. (2015). Graphene, related two dimensional crystals, and hybrid systems for energy conversion and storage. *Science, 347*(6217), 1246501.

Burgelman, M., Nollet, P., & Degrave, S. (2000). Modelling polycrystalline semiconductor solar cells. *Thin Solid Films, 361–362*, 527–532.

Burgelman, M., Decock, K., Khelifi, S., & Abass, A. (2013). Advanced electrical simulation of thin film solar cells. *Thin Solid Films, 535*, 296–301.

Cui, Y., Yao, H., Zhang, J., Zhang, T., Wang, Y., Hong, L., … & Hou, J. (2019). Over 16% efficiency organic photovoltaic cells enabled by a chlorinated acceptor with increased open-circuit voltages. *Nature Communications, 10*, 2515.

Decock, K., Khelifi, S., & Burgelman, M. (2011). Modelling multivalent defects in thin film solar cells. *Thin Solid Films, 519*(21), 7481–7484.

Ellmer, K. (2012). Past achievements and future challenges in the development of optically transparent electrodes. *Nature Photonics, 6*(12), 809–817.

Green, M. A., Dunlop, E. D., Hohl-Ebinger, J., Yoshita, M., Kopidakis, N., & Hao, X. (2021). Solar cell efficiency tables (version 58). *Progress in Photovoltaics: Research and Applications, 29*(7), 657–667.

Hall, R. N. (1952). Electron hole recombination in germanium. *Physical Review, 87*(2), 387.

Hau, S. K., Yip, H.-L., Baek, N. S., Zou, J., O'Malley, K., & Jen, A. K.-Y. (2008). Air stable inverted flexible polymer solar cells using zinc oxide nanoparticles as an electron-selective layer. *Applied Physics Letters, 92*(25), 253301.

Hou, J., Inganas, O., Friend, R. H., & Gao, F. (2018). Organic solar cells based on non fullerene acceptors. *Nature Materials, 17*(2), 119–128.

Hu, L., Liu, Y., Mao, L., Xiong, S., Sun, L., Zhao, N., … & Chen, Y. (2019). Chemical reaction between an ITIC type non fullerene acceptor and an amine containing interfacial layer. *ACS Applied Materials & Interfaces, 11*(30), 27295–27302.

Koo, D., Jung, S., Seo, J., Jeong, G., Choi, Y., Lee, J., … & Park, H. (2020). Flexible organic solar cells over 15% efficiency with polyimide-integrated graphene electrodes. *Joule, 4*, 1021–1034.

Kumar, A., & Zhou, C. (2010). The race to replace tin doped indium oxide: Which material will win? *ACS Nano, 4*(1), 11–14.

Li, G., Zhu, R., & Yang, Y. (2012). Polymer solar cells. *Nature Photonics, 6*(3), 153–161.

Lin, Y., Wang, J., Zhang, Z.-G., Bai, H., Li, Y., Zhu, D., & Zhan, X. (2015). An electron acceptor challenging fullerenes for efficient polymer solar cells. *Advanced Materials, 27*(7), 1170–1174.

Liu, Z., Li, J., & Yan, F. (2012). The application of highly doped single layer graphene as the top electrodes of semitransparent organic solar cells. *ACS Nano, 6*(1), 810–818.

Muzammil, M., Naam, K. N., Fareed, M., Hussain, M. S., & Zulfiqar, M. (2024). Boosting the performance of PBDB T/ITIC based organic solar cell: A theoretical analysis utilising SCAPS 1D. *Chemical Physics Impact, 8*, 100407.

Nithya, K. S., & Sudheer, K. S. (2020). Device modelling of non fullerene organic solar cell with inorganic CuI hole transport layer using SCAPS 1 D. *Optik, 217*, 164790.

Nithya, K. S., & Sudheer, K. S. (2022). Device modelling and optimisation studies on novel ITIC OE-based non-fullerene organic solar cell with diverse hole and electron transport layers. *Optical Materials, 123*, 111912.

Nowsherwan, G. A., Samad, A., Iqbal, M. A., Mushtaq, T., Hussain, A., Malik, M., Haider, S., Pham, P. V., & Choi, J. R. (2022). Performance analysis and optimization of a PBDB-T:ITIC-based organic solar cell using graphene oxide as the hole transport layer. *Nanomaterials, 12*(10), 1767.

Ouyang, J. (2013). Solution processed PEDOT: PSS films with conductivities as indium tin oxide through a treatment with mild and weak organic acids. *ACS Applied Materials & Interfaces, 5*(24), 13082–13088.

Park, H., Rowehl, J. A., Kim, K. K., Bulovic, V., & Kong, J. (2014). Flexible graphene electrode based organic photovoltaics with record high efficiency. *Nano Letters, 14*(9), 5148–5154.

Shockley, W., & Read, W. T. (1952). Statistics of the recombinations of holes and electrons. *Physical Review, 87*(5), 835–842.

Sun, Y., Seo, J. H., Takacs, C. J., Seifter, J., & Heeger, A. J. (2011). Inverted polymer solar cells integrated with a low temperature annealed sol gel derived ZnO film as an electron transport layer. *Advanced Materials, 23*(14), 1679–1683.

Yan, C., Barlow, S., Wang, Z., Yan, H., Jen, A. K.-Y., Marder, S. R., & Zhan, X. (2018). Non fullerene acceptors for organic solar cells. *Nature Reviews Materials, 3*, 18003.

Yuan, J., Zhang, Y., Zhou, L., Zhang, G., Yip, H.-L., Lau, T.-K., … & Zou, Y. (2019). Single junction organic solar cell with over 15% efficiency using fused ring acceptor with electron deficient core. *Joule, 3*(4), 1140–1151.

Zhao, W., Li, S., Yao, H., Zhang, S., Zhang, Y., Yang, B., & Hou, J. (2017). Molecular optimisation enables over 13% efficiency in organic solar cells. *Journal of the American Chemical Society, 139*(21), 7148–7151.

Zhao, W., Qian, D., Zhang, S., Li, S., Inganäs, O., Gao, F., & Hou, J. (2016). Fullerene free polymer solar cells with over 11% efficiency and excellent thermal stability. *Advanced Materials, 28*(23), 4734–4739.

Zheng, Z., Yao, H., Ye, L., Xu, Y., Zhang, S., & Hou, J. (2020). PBDB T and its derivatives: A family of polymer donors enables over 17% efficiency in organic photovoltaics. *Materials Today, 35*, 115–130.

APPENDIX

Table A1: Complete N_t sweep dataset for PM6:ITIC defect density tolerance analysis (active layer 100 nm, all other parameters at their baseline values)

$N_t (cm^{-3})$	V_{oc} (V)	J_{sc} ($mA\,cm^{-2}$)	FF (%)	PCE (%)
1×10^{12} (ideal baseline)	0.871	17.77	76.0	11.76
2×10^{12}	0.86	19.1	75.89	12.68
5×10^{12}	0.87	19.1	75.88	12.68
1×10^{13}	0.87	19.1	75.88	12.68
2×10^{13}	0.87	19.1	75.87	12.68
5×10^{13}	0.87	19.1	75.84	12.67
1×10^{14}	0.87	19.1	75.78	12.66
2×10^{14}	0.87	19.1	75.68	12.64
5×10^{14}	0.87	19.1	75.38	12.58
1×10^{15}	0.87	19.1	74.87	12.48
5×10^{15}	0.87	19.1	71.75	11.75
7×10^{15}	0.87	19.1	69.48	11.43
1×10^{16}	0.86	19.07	67.14	10.90
2×10^{16} (adopted)	**0.839**	**17.71**	**60.6**	**9.01**
3×10^{16}	0.83	19.01	55.81	8.83
5×10^{16}	0.81	18.95	49.07	7.57
1×10^{17}	0.78	18.8	40.8	6.02

Table A2: Complete active-layer thickness sweep dataset ($N_t = 2 \times 10^{16} cm^{-3}$, all other parameters at baseline)

$Thickness\ (nm)$	V_{oc} (V)	J_{sc} ($mA\,cm^{-2}$)	FF (%)	PCE (%)
50	0.826	10.88	67.71	6.09
80	0.836	15.35	63.13	8.1
100	0.839	17.71	60.6	9.01
120	0.841	19.68	58.35	9.65
140	0.841	21.3	56.31	10.09
150	0.841	22	55.36	10.24
160	0.84	22.63	54.45	10.35
170	0.84	23.19	53.58	10.44
180	0.84	28.69	52.75	10.49
190	0.84	24.12	51.95	10.51
200	0.84	24.53	51.19	10.52
220	0.84	25.15	49.76	10.47
250	0.833	25.77	47.83	10.27